LA-UR- 08-8031

Approved for public release;
distribution is unlimited.

Title:	Study of Two Tantalum Impact Specimens Using Experiments and Stochastic Polycrystal Plasticity Simulation
Author(s):	Michael R. Tonks- T3
Intended for:	International Journal of Plasticity

Los Alamos
NATIONAL LABORATORY
EST. 1943

Form 836 (7/06)

Study of Two Tantalum Taylor Impact Specimens Using Experiments and Stochastic Polycrystal Plasticity Simulation

Michael R. Tonks, John F. Bingert, Eric N. Harstad, Daniel A. Tortorelli

Abstract

We compare the experimentally obtained response of two cylindrical tantalum Taylor impact specimens. The first specimen is manufactured using a powder metallurgy (P/M) process with a random initial texture and relatively equiaxed crystals. The second is sectioned from a round-corner square rolled (RCSR) rod with an asymmetric texture and elongated crystals. The deformed P/M specimen has an axisymmetric footprint while the deformed RCSR projectile has an eccentric footprint with distinct corners. Also, the two specimens experienced similar crystallographic texture evolution, though the RCSR specimen experienced greater plastic deformation. Our simulation predictions mimic the texture and deformation data measured from the P/M specimen. However, our RCSR specimen simulations over-predict the texture development and do not accurately predict the deformation, though the deformation prediction is improved when the texture is not allowed to evolve. We attribute this discrepancy to the elongated crystal morphology in the RCSR specimen which is not represented in our mean-field model.

1 Introduction

Meso-scale crystallographic texture, which evolves under finite plastic deformation, is an important aspect of the macro-scale anisotropic response of polycrystalline materials. The crystallographic texture evolves towards certain preferred orientations largely determined by the crystal structure and the imposed loading history. The evolving meso-scale texture influences the material behavior

and hence the macro-scale response of the polycrystalline body. Though many studies have been conducted to link the effects of crystallographic texture evolution to macro-scale material behavior, they have primarily focused on quasi-static rates of deformation. Here, we investigate the effect of crystallographic texture under dynamic loading.

In the Taylor impact test, first proposed by Taylor [1] as a simple means of estimating the dynamic strength of materials, a cylindrical specimen is projected at a rigid anvil at a high velocity. The specimen experiences a high strain rate ($\sim 10^4$ s^{-1}) and high plastic deformation at the impact surface but only elastic deformation at the free end. The large range of plastic deformation experienced by the specimen produces a large range of evolved texture. Hence, the Taylor test is a useful means of observing the effect of texture on macro-scale deformation under dynamic loading. In this work, we compare the experimentally obtained response of two tantalum specimens with disparate initial textures subjected to high velocity Taylor impacts. The first specimen is manufactured using a powder metallurgy (P/M) process such that its initial texture is random and the crystals are relatively equiaxed. The second is sectioned from an as-received round-corner square rolled (RCSR) rod with an asymmetric initial texture and elongated crystals.

We also model the Taylor impact experiments and determine the accuracy with which the simulations predict the evolving texture and the anisotropic specimen deformation. We employ the finite element (FE) method and a mean-field polycrystal plasticity material model to predict the influence of the meso-scale crystal response on the macro-scale material behavior.

To bridge the macro- and meso-scales, mean-field polycrystal plasticity models consider an aggregate of N crystals at a material point. They do not explicitly model each crystal but rather they consider the crystals in a mean-field sense. For each crystal c in the aggregate the meso-scale crystal model predicts the crystal Cauchy stress $\mathbf{T}^c$ given the crystal velocity gradient $\mathbf{L}^c$. The meso-scale stresses $\mathbf{T}^c$ are subsequently averaged to obtain the macro-scale Cauchy stress $\mathbf{T}$. However, in general, the macro-scale velocity gradient $\mathbf{L}$ is known, not the meso-scale crystal velocity gradients $\mathbf{L}^c$. Consequently, a scheme is needed to map the macro-scale $\mathbf{L}$ to the meso-scale $\mathbf{L}^c$. Several models to this effect appear in the literature, the most common being the fully constrained model (FCM), based on the hypothesis in Taylor [2] that the crystal deformations are

equal to the macroscopic deformation, i.e. $\mathbf{L}^c = \mathbf{L}$. Although many applications of the FCM seem to validate its use (e.g. [3, 4]), it does not maintain equilibrium in the aggregate; however, it does provide an upper bound on the work necessary to achieve the macro-scale velocity gradient $\mathbf{L}$ [5]. In contrast, the no-constraints model (NCM) assumes a homogeneous stress in the aggregate [6], i.e. $\mathbf{T}^c = \mathbf{T}$, but does not ensure compatibility. Hence, the NCM provides a lower bound on the work [5]. Several alternative, less restrictive methods have been proposed [7–12], though their increased complexity comes at the expense of additional computation. In the stochastic Taylor model (STM) presented Tonks et al. [13], the $\mathbf{L}^c$ are obtained by randomly perturbing the macro-scale $\mathbf{L}$ according to tensor normal distributions. The STM is only slightly less efficient than the FCM and has been shown to predict the texture development in tantalum compression experiments more accurately than the FCM [13].

Two approaches have been suggested in the literature to incorporate mean-field polycrystal aggregate models into FE simulations. The most efficient is to construct a macro-scale microstructure-driven yield surface with the mean-field aggregate model [14–17]. The yield surface is then used in a phenomenological macro-scale plasticity analysis. Alternatively, the mean-field aggregate model can be used directly at each material integration point in the FE mesh to predict the material response [18–24]. In this way, the crystal responses directly influence the macro-scale response. Since the computational expense of the latter approach is high, it is generally used in conjunction with the efficient FCM [18, 20–24].

We model the response of the two Taylor impact specimens with FE simulations using a mean-field polycrystal aggregate model at each material point. In the simulations, the STM is used to approximate the crystal deformations rather than the FCM. Kothari and Anand [25] conduct a similar simulation of a Taylor impact specimen taken from a tantalum plate with an orthotropic initial texture. They consider 18 crystals in each material point aggregate and approximate the crystal deformations using the FCM. Their simulation predicts the macroscopic deformation of the specimen with reasonable accuracy, but they do not investigate the accuracy of the predicted texture development.

We begin in Section 2 by describing the two tantalum Taylor impact specimens and summa-

rizing the experiment. Then, in Section 3 we discuss the simulation method and determine the number of crystals required to accurately represent each material point aggregate. In Section 4, the experimental and simulation results are compared. We show that the two deformed specimens have dissimilar footprints and that they experienced similar texture evolution, though the RCSR specimen experienced greater plastic deformation. Our simulation predictions mimic the texture and deformation data measured from the P/M specimen. However, our RCSR specimen simulations over-predict the texture development and do not accurately predict the specimen deformation, though the deformation prediction is improved when the texture is not allowed to evolve. Finally, in Section 5 we discuss the behavior observed in both the experiments and the simulations. Particularly, we attribute the inability of the simulations to accurately predict the response of the RCSR specimen to its elongated initial crystal morphology which is not represented by our mean-field model.

2 Experiment Description

We compare the response of two 30 caliber (7.62 mm diameter), 2.0 in. long (50.8 mm) cylindrical tantalum specimens. The powder metallurgy (P/M) specimen is fabricated by cold isostatically pressing standard grade (687 ppm oxygen) tantalum powder into a cylindrical form at 345 MPa, and sintering at 2400°C in vacuum for one hour. This is followed by hot isostatically pressing the sintered blank at 1600°C and 207 MPa for 2 hours, resulting in a final density of 99.5% theoretical. The specimen is machined from the pressing. Due to the P/M process, the crystals comprising the specimen are relatively equiaxed with a random initial crystallographic texture.

The round-corner square rolled (RCSR) specimen is formed by the Cabot Co. by first radially forging a tantalum ingot under flat, orthogonally-opposed platens to a nominal diameter of 100 mm. The material is then round-corner square rolled followed by swaging to form the final rod. The as-received cylindrical rod is subjected to a recovery heat treatment at 800°C in order to restore adequate formability without affecting the initial texture before sectioning to form the specimen. Due to the asymmetric nature of much of its deformation processing, the RCSR specimen texture lacks the axisymmetry that is suggested by its cylindrical shape. The initial crystallographic texture

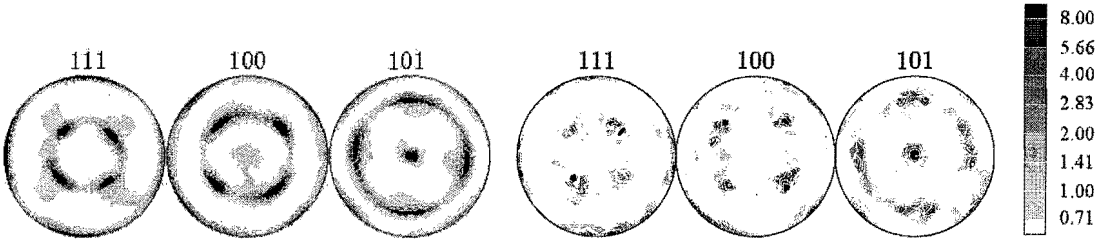

(a) Pole figures calculated from ODF measurement.

(b) Pole figures calculated from 1000 discrete orientations extracted from the ODF.

Figure 1: Pole figures of the asymmetric RCSR specimen initial texture measured using x-ray diffraction.

is composed of both a $\{110\}\langle 110\rangle$ component, referenced to an arbitrary radial direction, and a weaker $\{110\}\langle 001\rangle$ component (see Fig. 1(a) for pole figures of the RCSR specimen texture). The crystals comprising the RCSR specimen are highly elongated because of the tensile strain dominated processing, with an approximate crystal aspect ratio of 30:1 along the axial direction.

To represent the initial crystallographic textures for the simulations, we determine the orientation distribution function (ODF), i.e. the probability density function (PDF) of the orientations, of each specimen using X-ray diffraction measurements. Discrete orientations and corresponding weights representing their relative importance to the texture are extracted from the ODFs using the method outlined in Kocks et al. [26]. Sets of 1000 weighted orientations are extracted from the measured ODFs of the P/M and RCSR specimens (see Fig 1(b) for pole figures of the RCSR specimen texture calculated from the 1000 weighted orientations).

Maudlin et al. [27] investigate the RCSR specimen by generating a microstructure-driven yield surface describing the initial material response. The yield surface is generated with a mean-field polycrystal aggregate model of 1000 crystals using the FCM, i.e. $\mathbf{L}^c = \mathbf{L}$. They find strong coupling between the normal and shear stresses in the yield surface shape. This mixed-mode coupling produces a shearing deformation in the 1-2 plane of the RCSR specimen, where the axis is coincident with the compressive 3-axis.

Both specimens are deformed using a Helium gas-driven gun located at Los Alamos National Laboratory. They impact a highly polished AF1410 high strength steel anvil in medium vacuum conditions (10 Torr or 1.3 KPa) and are recovered after the test. The initial velocities of the

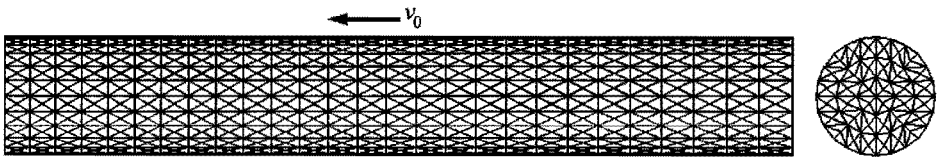

Figure 2: The finite element mesh of a tantalum impact specimen. The element axial lengths are biased such that an element at the specimen free end is 1.3 times longer than a corresponding element at the impact surface.

specimens are measured using a laser timing system. The P/M specimen is fired at $v_0 = 128$ m/s and the RCSR specimen is fired at $v_0 = 139$ m/s.

3 Simulation Method

In our Taylor impact simulations, the cylindrical specimens are represented with a 3-D mesh of 5,620 nodes and 23,328 tetrahedral elements (see Fig. 2). The axial length of the elements gradually decrease approaching the impact surface, such that an element at the free end of the specimen is 1.3 times longer than a corresponding element at the impact surface. The axial resolution of the elements was chosen to accurately describe the material response over most of the specimen while still maintaining a feasible computational cost; it is not sufficient to fully resolve the response near the impact surface. The Taylor impact is simulated with the FE code EPIC-06 which uses an explicit time stepping scheme and a Lagrangian kinematic description. We assume negligible impact-interface friction and a fully rigid anvil.

At each material point $\mathbf{x}$ and time instant t, the macroscopic applied velocity gradient $\mathbf{L}(t)$ is supplied to the material model which in turn calculates the resultant Cauchy stress $\mathbf{T}(t)$. Due to the high pressure that develops in the specimen, we require an equation of state (EOS) to represent the nonlinear pressure-volumetric strain response. Therefore we decompose the material stress response function into spherical and deviatoric components which are functions respectively of the spherical component $\frac{1}{3}\mathrm{tr}(\mathbf{L}(t))\mathbf{I}$ of $\mathbf{L}$ and the deviatoric component $\mathbf{L}'(t) = \mathbf{L}(t) - \frac{1}{3}\mathrm{tr}(\mathbf{L}(t))\,\mathbf{I}$, i.e.

$$\mathbf{T}(t) = \tilde{\mathbf{T}}'(\mathbf{L}'(t)) + \tilde{p}\left(\frac{1}{3}\mathrm{tr}(\mathbf{L}(t))\right)\mathbf{I}, \tag{1}$$

where p is the pressure, the tilde indicates response functions, and the prime denotes deviatoric components. The spherical component $\frac{1}{3}\text{tr}(\mathbf{L}(t))\,\mathbf{I}$ is used with the Mie-Grüneisen EOS [28] to calculate $p(t)$, where the EOS parameters for tantalum are taken from Walsh et al. [29].

The deviatoric aggregate Cauchy stress $\mathbf{T}'(t)$ is determined from $\mathbf{L}'(t)$ with a mean-field polycrystal plasticity model, i.e. we consider a polycrystal aggregate of N crystals at each material point. In the mean-field model we use the single crystal model presented in Tonks et al. [13] to compute the deviatoric crystal Cauchy stress $\mathbf{T}^{c\prime}(t)$ given the deviatoric crystal velocity gradient $\mathbf{L}^{c\prime}(t)$ for each of the N crystals in the aggregate. Then we calculate the deviatoric aggregate stress

$$\mathbf{T}'(t) = \sum_{c=1}^{N} w_c \mathbf{T}^{c\prime}(t), \tag{2}$$

where w_c is the weight extracted from the measured ODF of the material. We approximate $\mathbf{L}^{c\prime}(t)$ using the STM since it is nearly as computationally efficient as the FCM and it has been shown to predict textures that are more consistent with experiment than those predicted by the FCM [13].

In the STM [13], the deviatoric crystal strain rates $\mathbf{D}^{c\prime} = \frac{1}{2}(\mathbf{L}^{c\prime} + \mathbf{L}^{c\prime\mathrm{T}})$ are treated as normally distributed random tensors $\mathbf{D}^{c\prime}$ while the crystal spins $\mathbf{W}^c = \frac{1}{2}(\mathbf{L}^c - \mathbf{L}^{c\mathrm{T}})$ are equated to the aggregate spin $\mathbf{W} = \frac{1}{2}(\mathbf{L} - \mathbf{L}^{\mathrm{T}})$. Therefore $\mathbf{L}^{c\prime}$ is determined from a realization $\mathbb{D}^{c\prime}$ of the random tensor $\mathbf{D}^{c\prime}$ sampled in a Monte Carlo fashion, i.e. $\mathbf{L}^{c\prime} = \mathbb{D}^{c\prime} + \mathbf{W}$. The random tensors $\mathbf{D}^{c\prime}$ in each crystal are defined by the same second-order mean tensor $\boldsymbol{\mu}_{\mathbf{D}^{c\prime}} = \mathbf{D}'$, where $\mathbf{D}' = \frac{1}{2}(\mathbf{L}' + \mathbf{L}'^{\mathrm{T}})$, and the same fourth-order covariance tensor $\boldsymbol{\Sigma}_{\mathbf{D}^{c\prime}}$, which describe the statistical first- and second-moments. We assign the value of the covariance tensor $\boldsymbol{\Sigma}_{\mathbf{D}^{c\prime}}$ to define the behavior of $\mathbf{D}^{c\prime}$. Though $\boldsymbol{\Sigma}_{\mathbf{D}^{c\prime}}$ has 15 independent components, its assignment is simplified by assuming it to be isotropic and constant with time. The isotropic covariance tensor of the deviatoric $\mathbf{D}^{c\prime}$ is fully defined by the constant parameter σ_n^2, i.e.

$$\boldsymbol{\Sigma}_{\mathbf{D}^{c\prime}} = \sigma_n^2 \boldsymbol{\mathcal{S}} - \frac{1}{3}\sigma_n^2 \mathbf{I} \otimes \mathbf{I} \tag{3}$$

where $\boldsymbol{\mathcal{S}}$ is the fourth-order symmetrizer such that $\boldsymbol{\mathcal{S}}\mathbf{A} = \frac{1}{2}(\mathbf{A} + \mathbf{A}^{\mathrm{T}})$. We employ the value $\sigma_n^2 = (0.16\|\mathbf{D}'\|)^2$, where $\|\mathbf{D}'\| = \sqrt{\text{tr}(\mathbf{D}'^{\mathrm{T}}\mathbf{D}')}$ is the norm of $\mathbf{D}'$, which was determined in Tonks et al.

[13] by fitting predicted textures to textures measured from tantalum compression experiments.

The realizations $\mathbb{D}^{c\prime}$ in each material point aggregate are not generated randomly at each time step during the FE simulation. Rather, they are calculated from realizations $\mathbb{N}^{c\prime}$ of the normally distributed random tensor $\mathbf{N}'$ with mean tensor $\boldsymbol{\mu}_{\mathbf{N}'} = \mathbf{0}$ and covariance tensor $\boldsymbol{\Sigma}_{\mathbf{N}'} = \boldsymbol{\Sigma}_{\mathbf{D}^{c\prime}}$ (cf. Eq. (3)) according to

$$\mathbb{D}^{c\prime}(t) = \mathbb{N}^{c\prime} + \mathbf{D}'(t). \tag{4}$$

As seen in Eq. (4), the realization $\mathbb{N}^{c\prime}$ is constant, though $\mathbb{D}^{c\prime}(t)$ will change with time as $\mathbf{D}'(t)$ varies. The values of $\mathbb{N}^{c\prime}$ are generated at time $t = 0$ for the N crystals in each material point aggregate throughout the FE mesh.

The orientations of the N crystals in a material point aggregate define the crystallographic texture at that material point. The initial values for the orientations are taken from the two sets of 1000 weighted orientations extracted from the measured ODFs of the two specimens. The $N \leq 1000$ initial weighted orientations can be assigned deterministically, choosing the N orientations with the largest weights, or randomly according to the ODF. When the initial weighted orientations are assigned deterministically, the same initial orientations are used at every material point and therefore there is no spatial variability of the initial mechanical properties throughout the specimen. In contrast, when they are assigned randomly there is spatial variation of the initial mechanical properties but the initial texture is not represented as accurately as it would be with deterministic assignment. Beaudoin et al. [20] show that FE simulations in which the initial orientations are assigned randomly predict slower texture evolution than FE simulations in which the orientations are assigned deterministically, where this retardation effect increases with decreasing N.

In our simulation of the P/M specimen impact, we use the ODF to randomly assign the initial orientations at each material point. Since the initial texture is random, assigning the orientations randomly does not decrease the accuracy with which the texture is represented. However, we simulate the RCSR specimen impact twice; in one simulation the initial orientations are assigned deterministically and in the other they are assigned randomly. We compare the predicted behaviors to determine which assignment method predicts the specimen behavior more accurately.

At each time step and material point, the single crystal model determines $\mathbf{T}^{c\prime}$ and the evolution of the state variables, i.e. the crystal orientation $\mathbf{R}^c$ (represented by three Euler angles for each crystal), the crystal temperature, and the slip system flow stresses (we employ the $\{110\}\langle 111\rangle$ and $\{112\}\langle 111\rangle$ slip systems resulting in 24 total systems) for each of the N crystals in the material point aggregate. Since these calculations are performed for every material point aggregate at every integration point in the FE mesh, $23,328 \times N$ nonlinear crystal simulations are conducted at each time step after which the $23,328 \times 28 \times N$ state variables are stored. Hence, the computational expense of a simulation is high. Although, the expense can be lessened by reducing the value of N. Such a reduction could adversely affect the accuracy of the predicted response; therefore a tradeoff is made between accuracy and computational expense.

To determine a value of N that is an adequate compromise between accuracy and computational expense, we determine the accuracy of the mean-field polycrystal plasticity model with increasing values of N. The model accuracy is determined by calculating the deviatoric aggregate stress $\mathbf{T}'$ and the evolved crystal orientations in a tantalum polycrystal aggregate subjected to the applied velocity gradient

$$\mathbf{L}' = \begin{bmatrix} 500 & 0 & 0 \\ 0 & 500 & 0 \\ 0 & 0 & -1000 \end{bmatrix} \mathrm{s}^{-1} \tag{5}$$

for a single time step $\mathrm{d}t = 1.0 \times 10^{-3}$ s. Note that this is not a full FE calculation but rather a single material point calculation using the polycrystal plasticity model with $N \leq 1000$ crystals. Due to the stochastic nature of the $\mathbf{L}^{c\prime}$ approximated by the STM, we repeat the calculation ten times with the same N initial orientations and calculate the average stress $\mathbf{T}'$ and the average evolved crystal orientations $\mathbf{R}^c$. We then compare the average stress and crystal orientations to those computed from similar calculations using the full set of 1000 orientations extracted from the measured ODFs. We quantify the difference between the predicted stresses with the error function

$$\mathrm{err}_{\mathbf{T}} = \frac{|\sigma_{v\,0} - \sigma_{v\,N}|}{\sigma_{v\,0}}, \tag{6}$$

where the subscript 0 denotes the values calculated using the full set of 1000 orientations and σ_v is the von Mises stress calculated from $\mathbf{T}'$. We quantify the difference between the predicted crystal orientations by first calculating pole figures, i.e. the concentration of crystal poles that intersect a point on a hemisphere defined by the angles ϕ and θ. We then calculate the average pole figure error according to

$$\mathrm{err}_{\mathrm{PF}} = \frac{1}{3}\left(\mathrm{err}_{\mathrm{PF}}^{100} + \mathrm{err}_{\mathrm{PF}}^{101} + \mathrm{err}_{\mathrm{PF}}^{111}\right), \tag{7}$$

where, e.g.

$$\mathrm{err}_{\mathrm{PF}}^{100} = \frac{\int_0^{\pi}\int_0^{\frac{\pi}{2}} \left|p_0^{100}(\phi,\theta) - p_N^{100}(\phi,\theta)\right| \sin(\theta)\,\mathrm{d}\theta\,\mathrm{d}\phi}{\int_0^{\pi}\int_0^{\frac{\pi}{2}} \left|p_0^{100}(\phi,\theta)\right| \sin(\theta)\,\mathrm{d}\theta\,\mathrm{d}\phi} \tag{8}$$

with $p^{100}(\phi,\theta)$ the concentration of $\{100\}$ poles at a specific ϕ and θ.

For the P/M specimen, we determine the accuracy of the mean-field polycrystal plasticity model with increasing values of $N \leq 1000$ using random assignment of the initial orientations. From the calculated stress and pole figure errors ($\mathrm{err}_{\mathbf{T}}$ and $\mathrm{err}_{\mathrm{PF}}$, respectively) shown in Fig 3(a), we determine that $N = 200$ is a reasonable compromise between accuracy and computational expense. For the RCSR specimen we evaluate the errors using both deterministic and random initial orientation assignment. As expected, deterministic assignment results in lower pole figure error than random assignment, however deterministic assignment only results in lower stress error for $N > 400$ (see Fig. 3(b) for the error curves from the RCSR specimen texture). Again, $N = 200$ appears to be a good compromise between accuracy and computational expense for both random and deterministic initial orientation assignment. Therefore we use $N = 200$ crystals in each material point aggregate for the P/M specimen simulation and both RCSR specimen simulations.

Both specimen impacts are simulated with the measured initial velocities for 1.1×10^{-4} s, after which time the plastic deformation quiesced. The simulations are conducted using the single crystal model parameter values for tantalum from Tonks et al. [13] except for the initial flow stress τ_{0_0} and the hardening parameter h_0, which differ between the P/M and RCSR specimen materials. Experimental data are not available to prescribe the values of τ_{0_0} and h_0 for the two specimens.

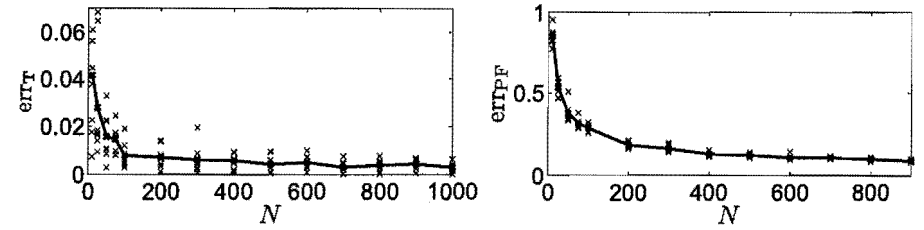

(a) Random P/M specimen initial texture

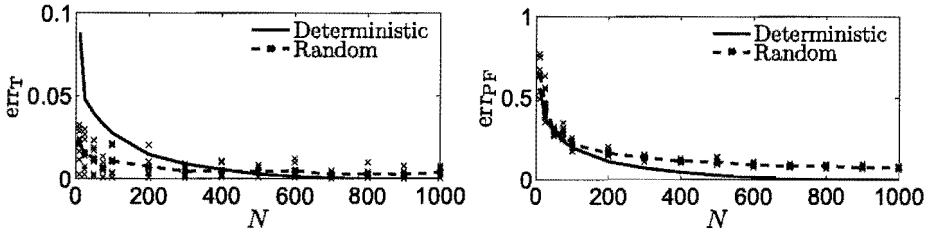

(b) RCSR specimen initial texture

Figure 3: The stress and pole figure error vs. N calculated from the average of 10 STM polycrystal plasticity simulations. For random orientation assignment, the points show the error for eight sets of STM runs with different initial orientations and the line is the average over the eight. $N = 200$ appears to be a good compromise between accuracy and computational expense.

Therefore, we prescribe their values by fitting the predicted deformed lateral cross-sections of the Taylor specimens to the lateral cross-sections of the recovered deformed specimens. In so doing, we determine that $\tau_{0_0} = 0.075$ GPa and $h_0 = 3.5$ GPa for the P/M specimen and $\tau_{0_0} = 0.05$ GPa and $h_0 = 3.5$ GPa for the RCSR specimen.

4 Experiment and Simulation Results

In this section we present the data from the two Taylor impact experiments. We also show the simulation predictions and compare them to the experimental data. In each case we begin by discussing the deformed shape of the specimens and then discuss the evolved texture.

The two recovered specimens have similar lateral cross-sections with three distinct regions of deformation, as seen in Fig. 4. Region A is highly deformed with a rapid diameter change, region B has a more gradual diameter change, and region C shows very little deformation. There is a pronounced transition from region A to region B which occurs 4 mm from the impact surface in both specimens. However, the transition from region B to region C is gradual and occurs

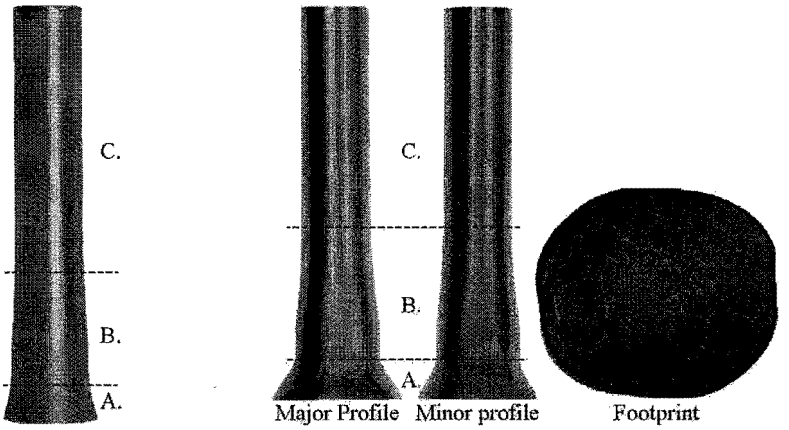

(a) P/M specimen.

(b) RCSR specimen, with the footprint shown at twice the scale of the major and minor profiles.

Figure 4: Photographs of the two deformed Taylor specimens. The three deformation regions are labeled in the figures.

approximately 16 mm from the impact surface in the P/M specimen and approximately 19 mm from the impact surface in the RCSR specimen. Note that while the P/M specimen simulation under-predicts the final length, it over-predicts the deformed radius such that the specimen volume is conserved throughout the simulation. The RCSR specimen experienced more deformation than the P/M specimen with a final length of 43.7 mm, while the P/M specimen has a final length of 45.8 mm. It is likely that the greater deformation experienced by the RCSR specimen is primarily due to its higher initial velocity. While their lateral cross-sections are similar, the two specimens have disparate footprints. The deformed P/M specimen has a circular footprint, while the deformed RCSR specimen has an eccentric footprint with pronounced corners. The axisymmetric deformation of the P/M specimen is expected because of its random initial texture and the axisymmetric nature of the loading.

The simulation of the P/M specimen over-predicts the macro-scale deformation, with a predicted final length of 43.3 mm in contrast to the measured length of 45.8 mm (see Fig. 5(a)). However, it accurately predicts the axisymmetric deformation. The two RCSR specimen simulations, i.e. the simulation in which the initial orientations are assigned deterministically and that in which they are assigned randomly, predict nearly identical specimen deformation. The predicted specimen footprints are elliptical without evidence of the eccentricity nor the distinct corners observed in

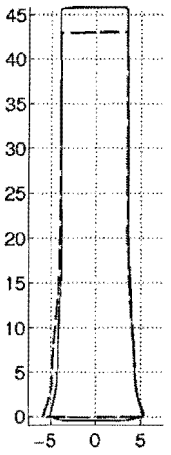

(a) P/M specimen profile.

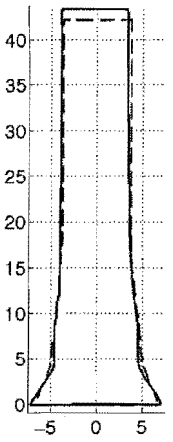

Major Profile

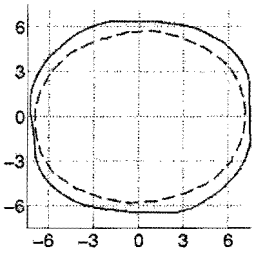

Footprint

(b) RCSR specimen with deterministic initial orientation assignment.

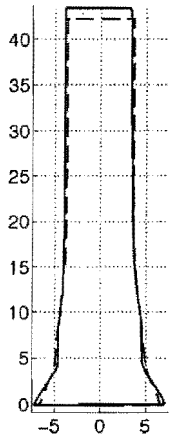

Major Profile

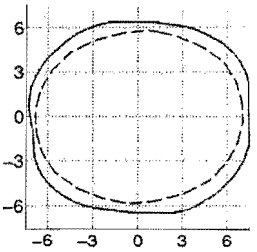

Footprint

(c) RCSR specimen with random initial orientation assignment.

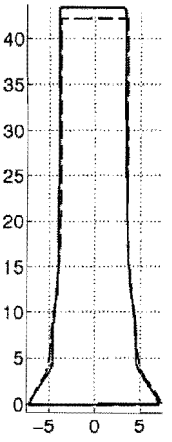

Major Profile

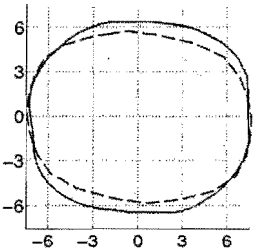

Footprint

(d) RCSR specimen with random initial orientation assignment and no texture evolution.

Figure 5: Comparison between the deformation predicted by simulation (dashed line) and measured from the recovered specimens (solid line) for the two tantalum specimens. The axes are labeled in mm.

the experiment (see Figs. 5(b) and 5(c)). Both simulations predict a deformed length of 42.5 mm while the measured length is 43.7 mm. The deformed lateral cross-sections of the two specimens are accurately predicted by all the simulations. This is due to our determining the values of the τ_{0_0} and h_0 material parameters by fitting the predicted deformed lateral cross-sections to the lateral cross-sections of the recovered specimens, as discussed in the previous section.

In the RCSR specimen simulation using a microstructure-driven yield surface conducted by Maudlin et al. [27], a more accurate deformed footprint is predicted when the texture is not allowed to evolve. Though they do not postulate a cause for this behavior, we investigate their findings by repeating the RCSR specimen simulation using random initial orientation assignment with the crystal orientations held constant. The resultant deformed footprint is more accurate than that predicted by the simulation in which the texture is allowed to evolve, capturing more of the eccentricity of the experimental footprint (see Fig. 5(d)). In Section 5 we discuss a probable cause for this behavior.

Texture measurements were made on various axis-normal sections along the recovered specimens (see Fig. 6 for experimental pole figures of the texture in the P/M specimen and Fig. 7 for experimental pole figures of the texture in the RCSR specimen). We quantify the texture evolution along the length of the specimens by calculating the pole figure error $\mathrm{err}_{\mathrm{PF}}$ (cf. Eq. (7)) between the initial specimen textures (cf. Fig. 1) and the measured post-loading textures (see Fig. 8). Note that the $\mathrm{err}_{\mathrm{PF}}$ does not differentiate between differences in texture strength and differences in the texture components, i.e. the $\mathrm{err}_{\mathrm{PF}}$ between two similar textures with different strengths could be equal to the $\mathrm{err}_{\mathrm{PF}}$ between two distinctly different textures. In the P/M specimen, a strong duplex $\langle 001 \rangle$ / $\langle 111 \rangle$ compression texture developed near the impact surface, as shown in Fig. 6. The duplex texture persists throughout the specimen, though the strength of the texture decreases with increasing axial distance from the impact surface. The texture evolution decreases rapidly away from the impact surface until it reaches a local minimum at 4 mm (cf. Fig. 8), which coincides with the transition from region A to region B in the lateral cross-section. Above 6 mm the texture evolution resumes decreasing, though the slope is more gradual.

The recovered RCSR specimen developed a $\langle 111 \rangle$ texture at the impact surface, which transi-

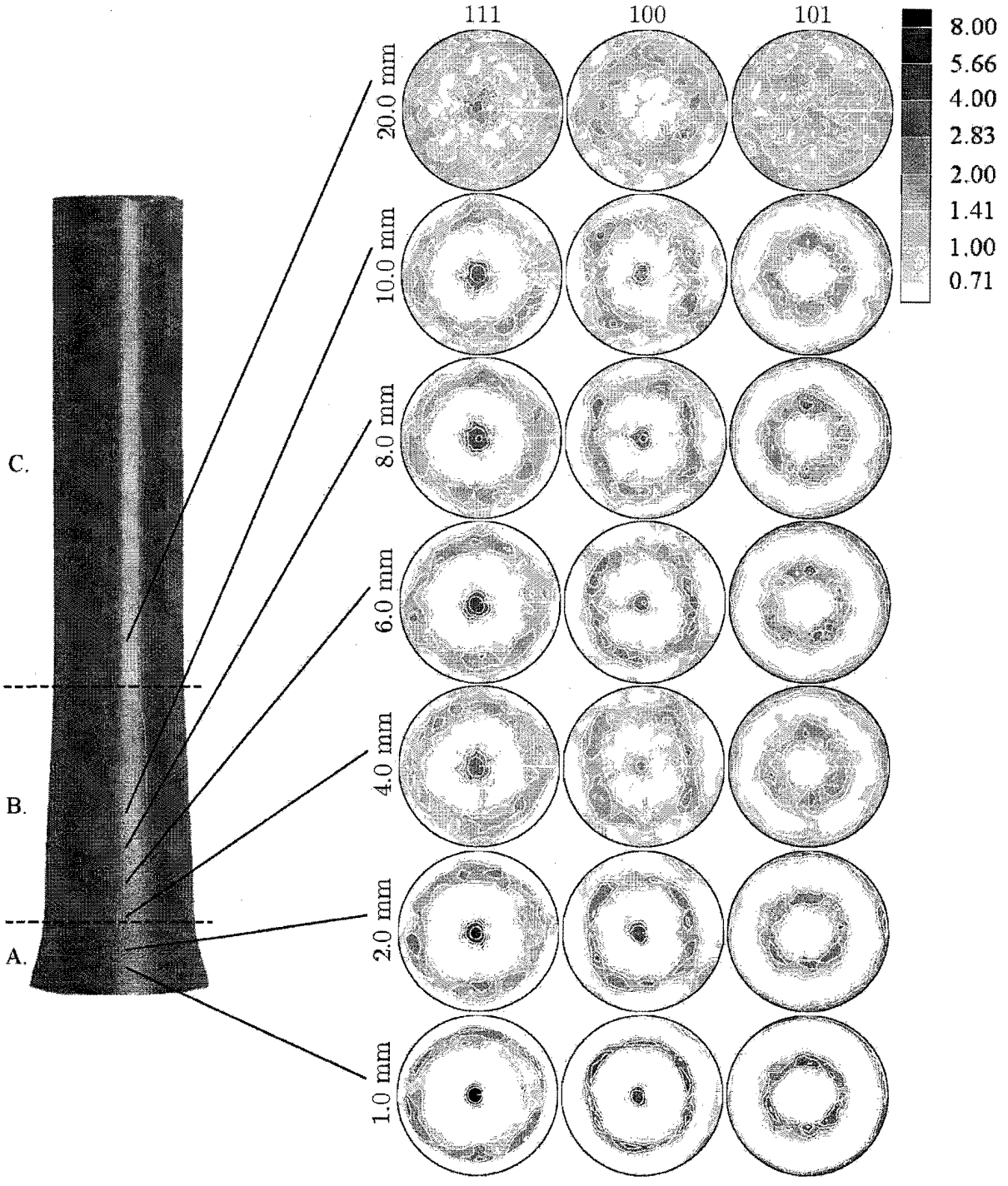

Figure 6: Pole figures of the texture measured along the recovered P/M specimen. The legend has units of multiples of random distribution (m.r.d.).

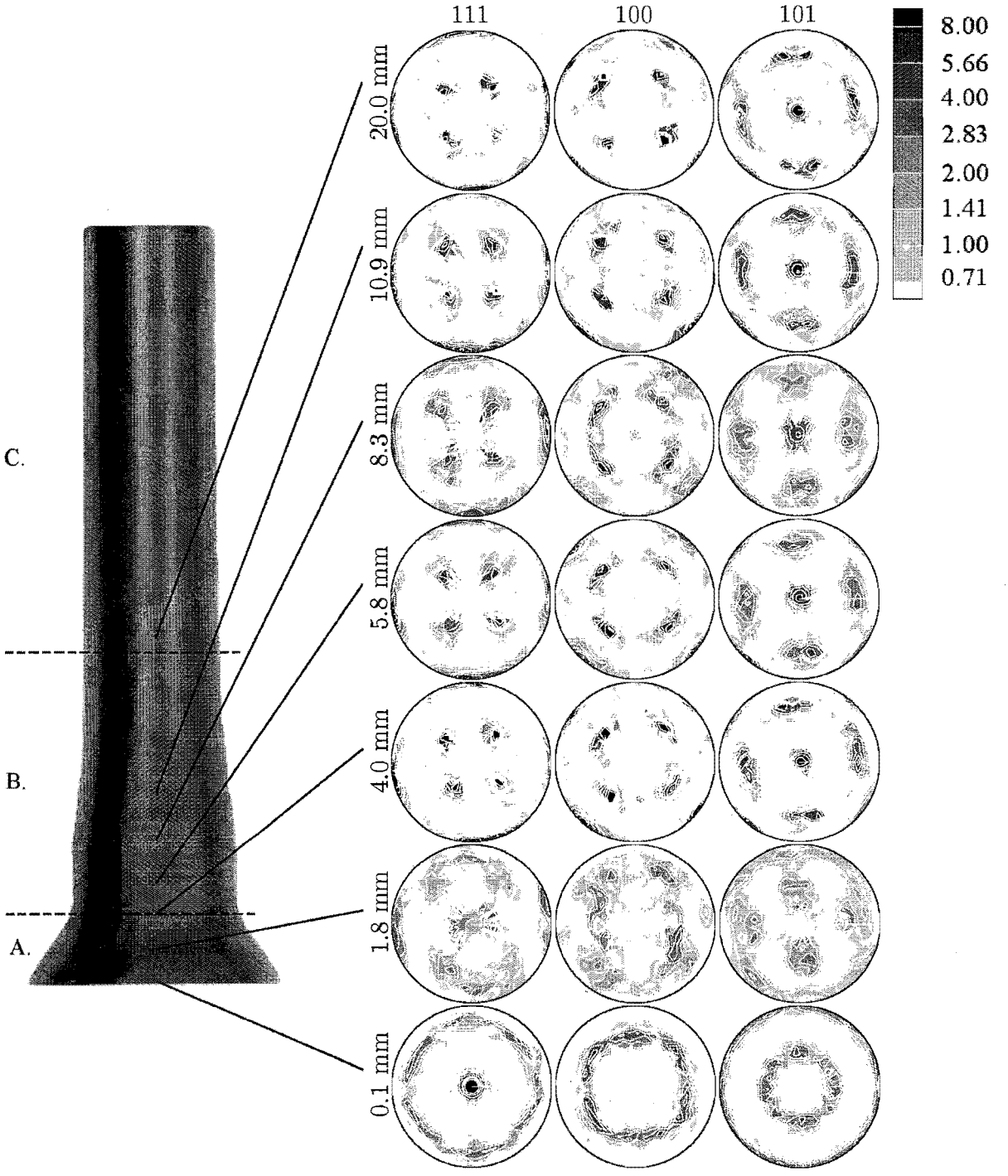

Figure 7: Pole figures of the texture measured along the recovered RCSR specimen. The legend has units of m.r.d.

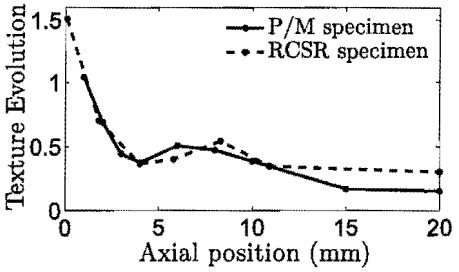

Figure 8: The texture evolution in the recovered specimens at the indicated axial positions, quantified by calculating the $\mathrm{err}_{\mathrm{PF}}$ (cf. Eq. (7)) between the measured initial and post-loading textures.

tions to a weakened form of the initial texture 20 mm from the impact surface (cf. Fig. 7). As in the P/M specimen, a local minimum in the texture evolution occurs at 4 mm (cf. Fig. 8), which coincides with the transition from region A to region B. By comparing the texture in the two specimens, we observe that the P/M and RCSR specimens experienced similar texture evolution as quantified by $\mathrm{err}_{\mathrm{PF}}$, though the RCSR specimen experienced greater plastic deformation. In addition, in the P/M specimen the $\langle 001 \rangle$ / $\langle 111 \rangle$ texture is evident 20 mm from the impact surface with the texture strength increasing nearer the impact surface. Conversely, the basic components of the initial RCSR specimen texture persist down to 4 mm from the impact surface, followed by a sharp transition to the $\langle 111 \rangle$ texture. The persistence of the initial RCSR texture, and the resultant delay in the development of the axisymmetric $\langle 111 \rangle$ texture, contributes to the development of the corners in the deformed specimen footprint.

As with the experimentally obtained texture, we plot pole figures of the simulated texture along the length of the two specimens (see Figs. 9, 10, and 11 for pole figures from the P/M specimen, the RCSR specimen with deterministic initial orientation assignment, and the RCSR specimen with random initial orientation assignment, respectively). We also quantify the texture evolution along the specimens as was done for the experiments (see Fig. 12). In addition, the error in the texture predictions is quantified by calculating the pole figure error $\mathrm{err}_{\mathrm{PF}}$ (cf. Eq. (7)) between the experimentally obtained and simulated textures (see Fig. 13).

The P/M specimen simulation predicts textures similar to those measured from the recovered specimen between 2 mm and 10 mm from the impact surface (see Figs. 9 and 13(a)). However, the simulation significantly under-predicts the strength of the texture near the impact surface. Also,

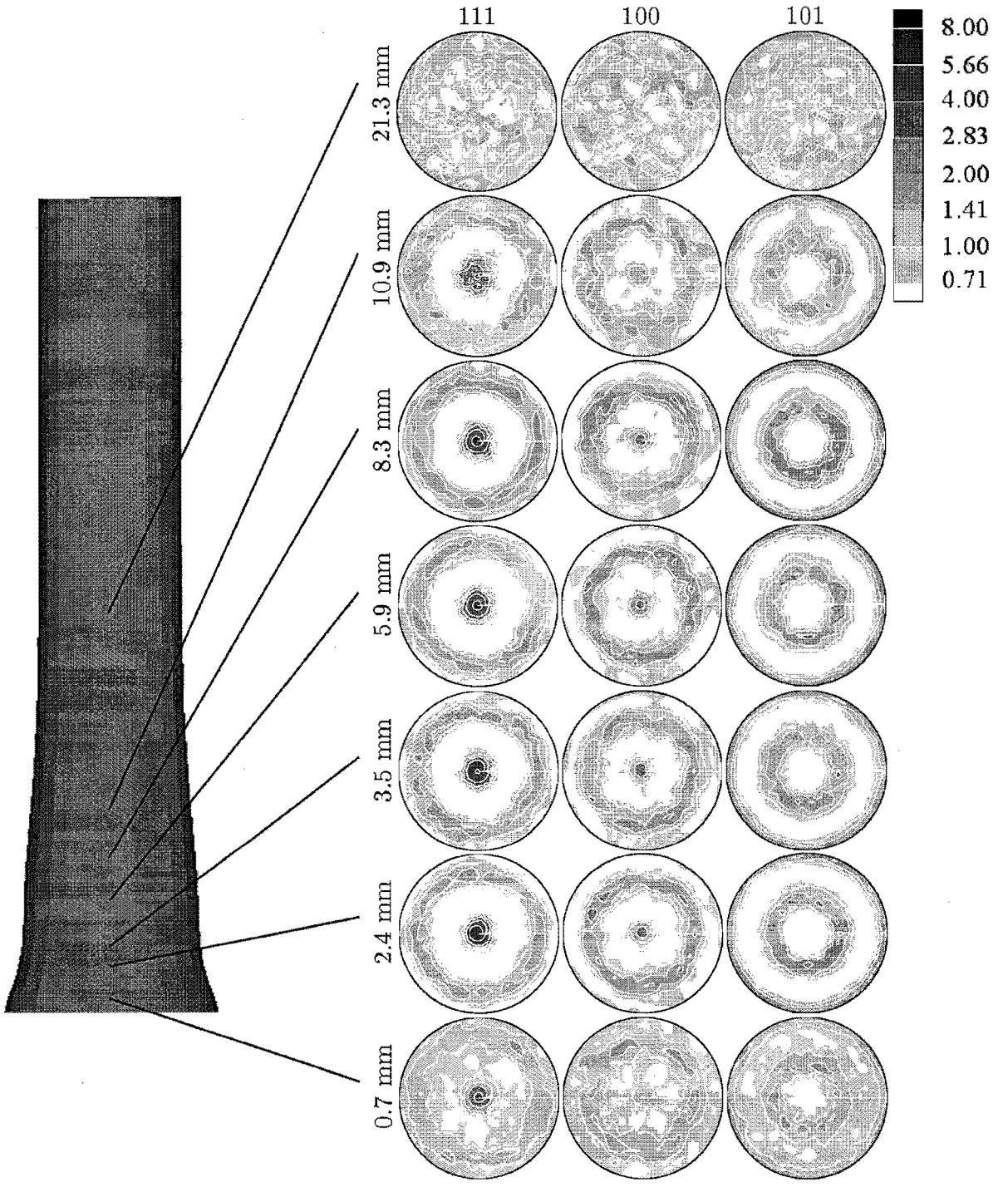

Figure 9: Pole figures of the predicted final texture along the P/M specimen. The legend has units of m.r.d.

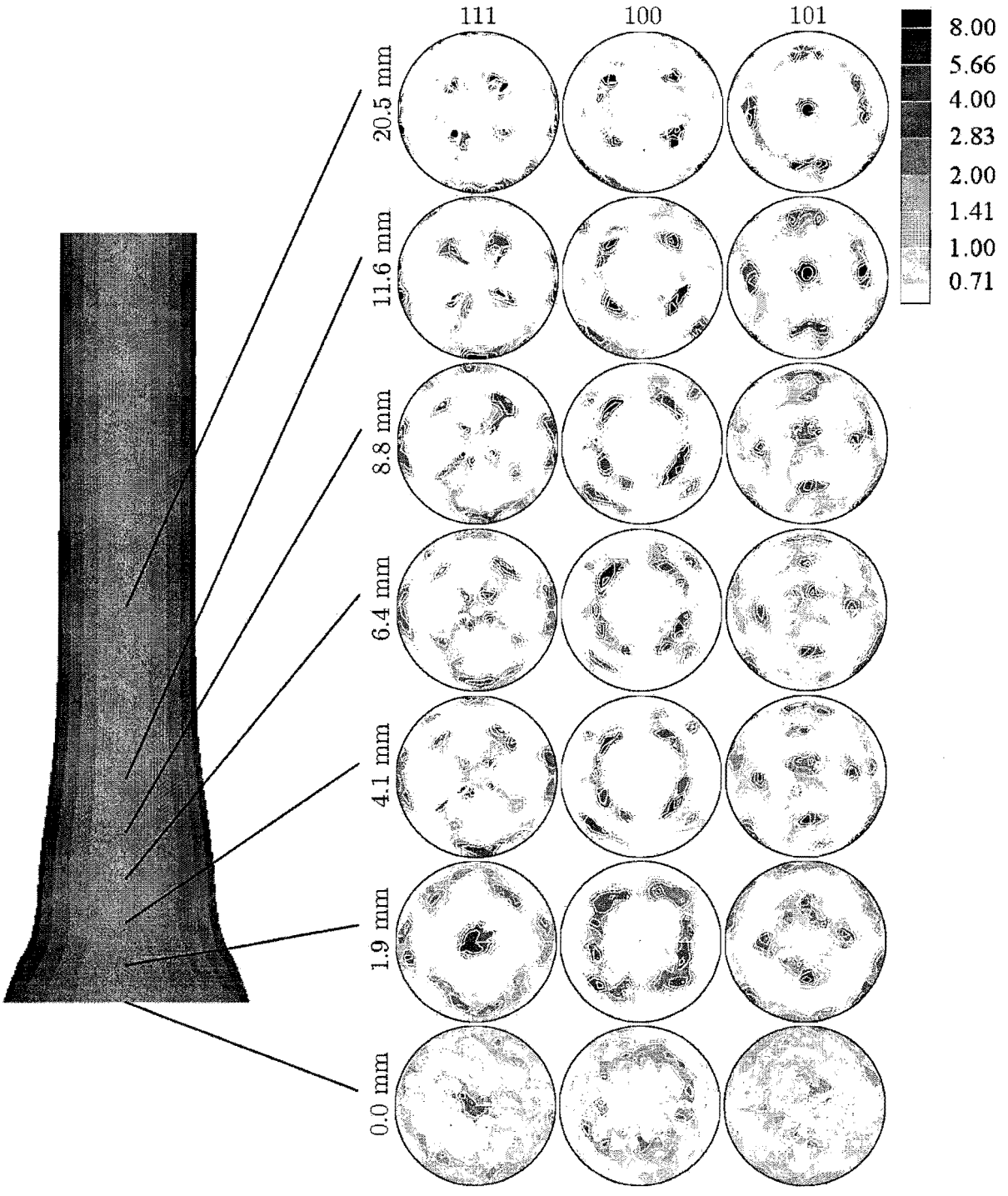

Figure 10: Pole figures of the predicted final texture along the RCSR specimen with deterministic initial orientation assignment. The legend has units of m.r.d.

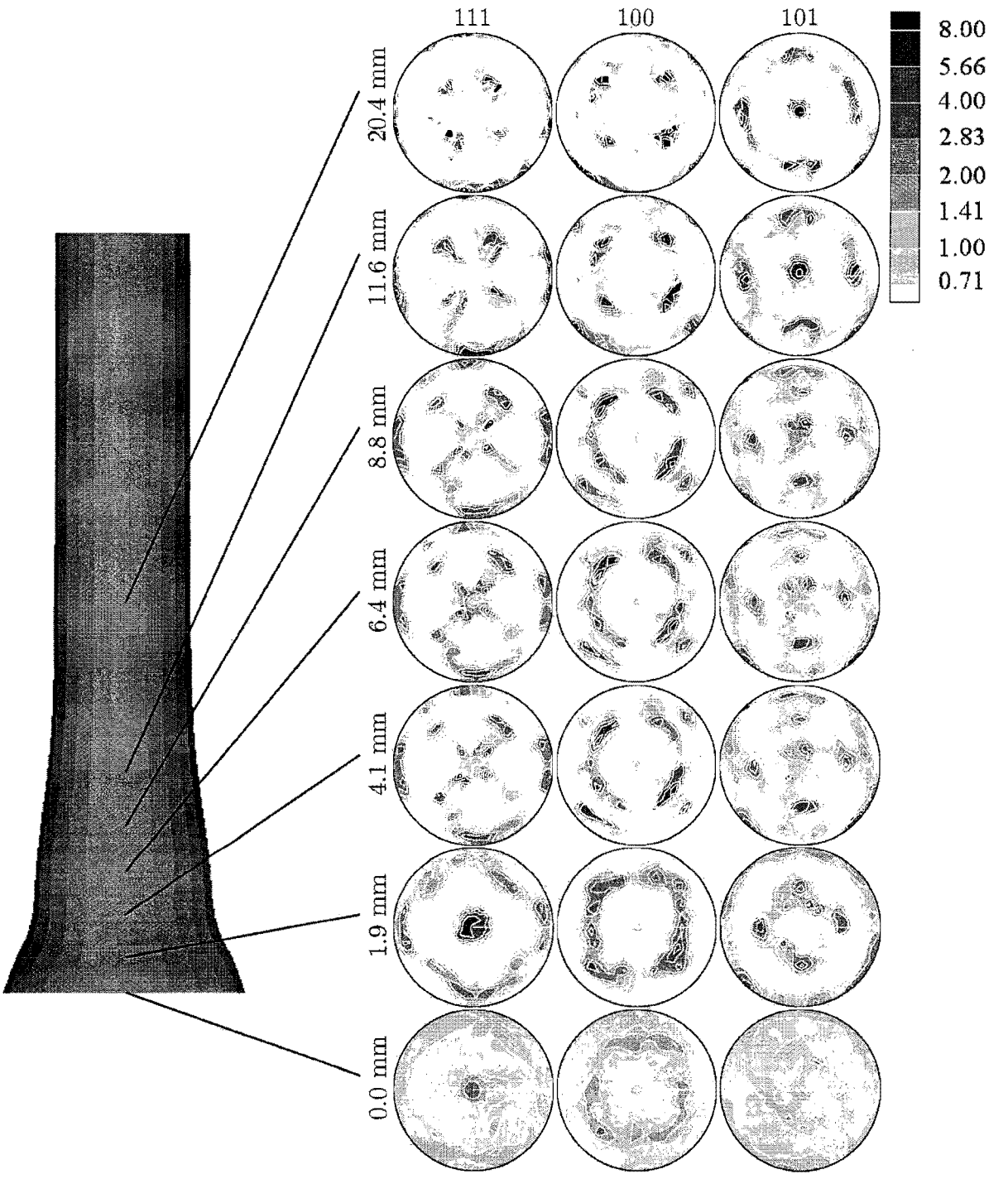

Figure 11: Pole figures of the predicted final texture along the RCSR specimen with random initial orientation assignment. The legend has units of m.r.d.

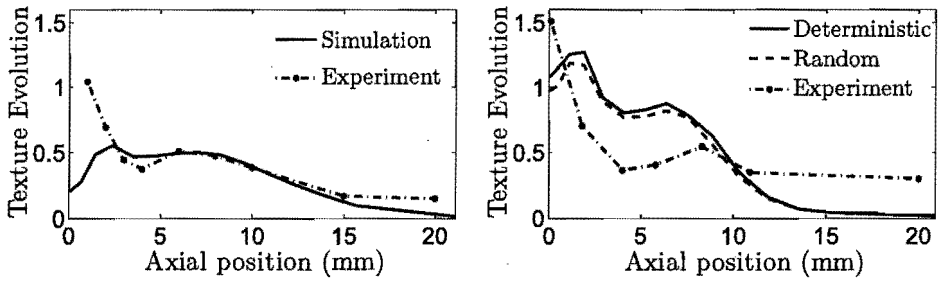

(a) P/M specimen (b) RCSR specimen

Figure 12: The texture evolution predicted by the simulations at the indicated axial positions, quantified by calculating the err_{PF} (cf. Eq. (7)) between the initial and predicted post-loading textures. The texture evolution curves from the experiments are shown for reference.

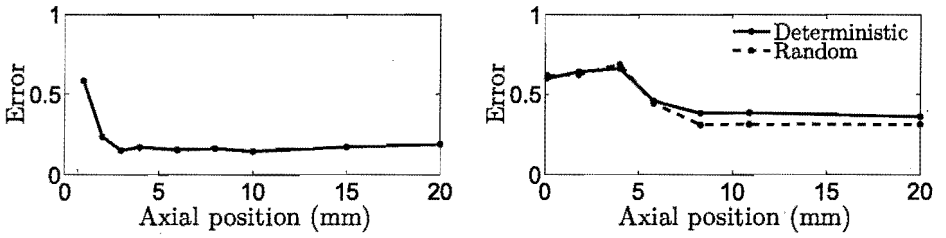

(a) P/M specimen (b) RCSR specimen

Figure 13: The error in the predicted textures at the indicated axial positions, quantified by calculating the err_{PF} (cf. Eq. (7)) between the experimentally obtained and simulated textures at corresponding axial positions.

the texture predicted 20 mm from the impact surface appears random, unlike the weak duplex $\langle 001 \rangle$ / $\langle 111 \rangle$ texture obtained from the experiment. Accordingly, the texture evolution predicted by the simulation between 2 mm and 10 mm is similar to that experienced by the recovered specimen but the evolution is under-predicted near the impact surface and above 10 mm from the impact surface (Fig. 12(a)). Note that a local minimum in the texture evolution is predicted 4 mm from the impact surface, though it is not a pronounced as that obtained in the experiment. We postulate that the decrease in the predicted texture evolution near the impact surface is due to insufficient mesh resolution within the finite element model at that location.

For the RCSR specimen, both simulations predict similar evolved textures, though the random initial orientation assignment simulation predicts slightly less texture evolution than the deterministic assignment simulation. The simulations predict a strong $\langle 111 \rangle$ texture with a very slight $\langle 001 \rangle$

component at the impact surface and a nearly unaltered initial texture 20 mm from the impact surface (cf. Figs. 10 and 11). Between 20 mm and the impact surface the predicted texture gradually transitions from the initial texture to the ⟨111⟩ texture, though the simulations predict significantly more texture evolution than was obtained in the experiment (cf. Fig. 12(b)). As with the P/M specimen simulation, the RCSR simulations predict a decrease in the texture evolution near the impact surface, probably due to insufficient mesh resolution. The local minimum in the texture evolution at 4 mm is again predicted. The error between the predicted and experimentally obtained textures increases with decreasing axial distance from the impact surface with a maximum at 4 mm (cf. Fig. 13(b)). Also, the random assignment simulation results in slightly less error than the deterministic assignment simulation. By comparing the errors from the P/M and RCSR specimen simulations (cf. Fig. 13), we note that the P/M specimen simulation predicts the texture more accurately than the RCSR specimen simulations.

5 Discussion

The RCSR specimen simulations employing deterministic and random initial orientation assignment predict similar bulk deformation. In addition, both simulations predict similar overly evolved textures, though the random assignment simulation predicts slightly less texture evolution. The small difference in the predicted texture evolution is not sufficient to recommend either initial orientation assignment method. However, Beaudoin et al. [20] show that the reduction in the texture evolution due to random assignment increases with decreasing N, i.e. the number of crystals in each material point aggregate. Therefore, the difference between deterministic and random initial orientation assignment may become significant for simulations with $N < 200$.

To further evaluate the effectiveness of using the STM material model in a Taylor specimen impact, we repeat the P/M specimen simulation using the FCM. The FCM simulation takes 85.1% as long as the STM simulation and predicts similar deformation but over-predicts the texture evolution (see Fig. 14 for the predicted texture evolution and the error between the experimentally obtained and predicted textures using the STM and the FCM). Therefore, the STM provides a 37% increase in accuracy over the FCM with only a 17% increase in computation time.

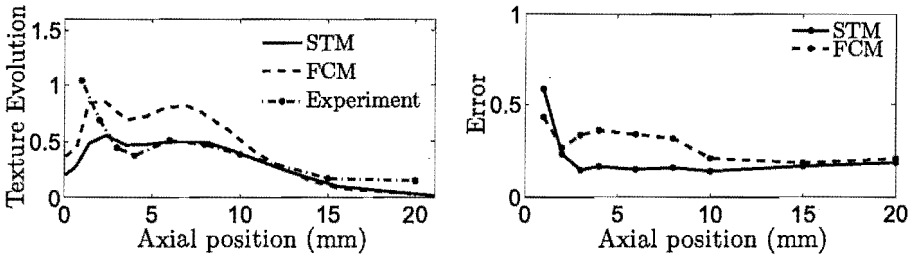

(a) The texture evolution predicted by the simulations, quantified as in Fig. 12.

(b) The error in the predicted textures, quantified as in Fig. 13.

Figure 14: Comparison of P/M specimen simulation predictions using the STM and the FCM, indicating that the STM is more accurate than the FCM.

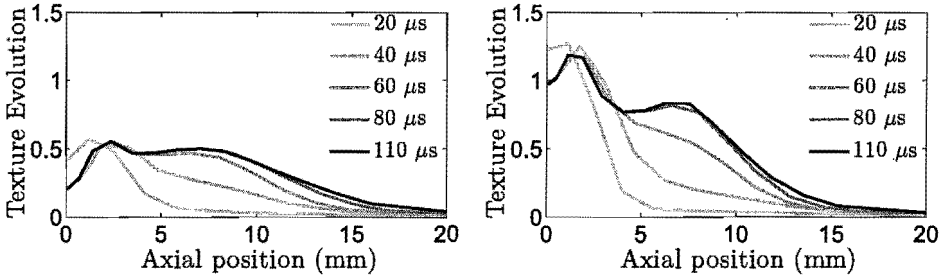

(a) P/M specimen

(b) RCSR specimen with randomly assigned initial orientations

Figure 15: The texture evolution predicted by the simulations at the indicated axial positions and the indicated times, quantified as in Fig. 13. The figures identify the time at which the local minimum in the texture evolution first occurs.

The different initial textures in the P/M and RCSR specimens resulted in the recovered P/M specimen having a circular footprint and the recovered RCSR specimen having an eccentric footprint with distinct corners. However, the general shapes of the lateral cross-sections were similar (cf. Fig. 4). Therefore, it appears that the initial texture affects the shape of the footprint but not the general shape of the lateral cross-section.

Both recovered tantalum specimens experienced a local minimum in the texture evolution 4 mm from the impact surface coinciding with the transition from region A to region B in the lateral cross-section (cf. Figs. 6, 7, and 8). This local minimum is also predicted by the simulations. To investigate the cause of the local minimum, we quantify the predicted texture evolution at various times during the simulations (see Fig. 15). For the RCSR specimen, we use the simulation with random initial orientation assignment which results in a slightly more accurate texture prediction.

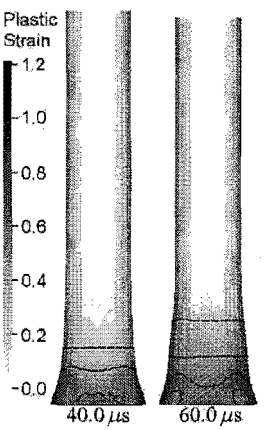

(a) P/M specimen.

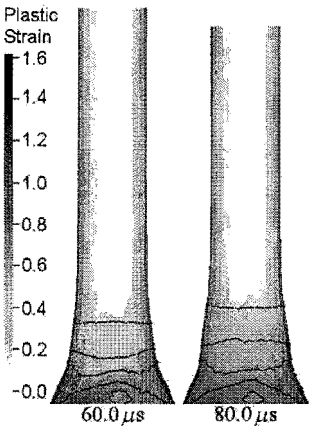

(b) RCSR specimen with randomly assigned initial orientations.

Figure 16: Simulated lateral cross-sections of the two specimens prior to and at the appearance of the local minimum in the texture evolution. Note that the appearance of the region B deformation coincides with the appearance of the local minimum.

The local minimum first appears in the simulations at 60 μs for the P/M specimen and at 80 μs for the RCSR specimen. The simulations predict that prior to the appearance of the local minimum there is no region B deformation, i.e. the specimen is highly deformed near the impact surface with little deformation further up the specimen (see Fig. 16 for the predicted lateral cross-sections of the specimens prior to and at the appearance of the local minimum). The appearance of the local minimum coincides with the appearance of the region B deformation, i.e. the more gradual diameter change above the highly deformed portion of the specimen. We postulate that the appearance of the region B deformation is due to the highly deformed material near the impact surface hardening sufficiently such that it no longer deforms. In essence, a new anvil of hardened tantalum forms which constrains the plastic deformation that occurs higher up the specimen. Due to compatibility, the material just above the hardened area is not sheared as much as the surrounding material. Therefore, its texture evolves less than that of the surrounding material.

The experimental texture in the RCSR specimen appears to be resistant to evolution, e.g. the P/M and RCSR specimens experienced similar texture evolution, though the P/M specimen experienced significantly less plastic deformation (cf. Fig. 8). In addition, it appears that this resistance to evolution is not captured by our mean-field polycrystal plasticity model since the RCSR

specimen simulations over-predict the texture evolution and predict the specimen deformation more accurately when the texture is not allowed to evolve (cf. Figs. 5(d) and 12(b)). A possible cause of this behavior is the highly elongated crystal morphology in the RCSR specimen. We surmise that as the specimen deforms, the crystal rotations are inhibited due to compatibility constraints between neighboring elongated crystals. Only near the impact surface, where the large plastic strain is sufficient to refine the microstructure, does significant texture evolution occur. Our mean-field polycrystal plasticity model does not predict this response because it does not consider crystal morphology. Finite element simulations in which each crystal is resolved by one or more elements may represent this behavior [18, 20, 30–32], but simulating the entire specimen with such a method would be extremely computationally expensive. The rotations of the P/M specimen crystals are not inhibited in this manner due to their equiaxed morphology.

6 Conclusions

We compared the experimentally obtained responses of P/M and RCSR tantalum Taylor impact specimens. The deformed P/M specimen has an axisymmetric footprint while the deformed RCSR specimen has an eccentric footprint with distinct corners. Also, the two specimens experienced similar texture evolution, though the RCSR specimen experienced greater plastic deformation. From these results we postulate that the initial texture affects the deformed footprint but not the deformed lateral cross-section.

We simulated the Taylor specimen impacts with the FE code EPIC-06 using a mean-field polycrystal material model in which the $\mathbf{L}^{c\prime}$ were approximated with the STM. The P/M specimen simulation predicts the texture and deformation data measured from the recovered specimen with reasonable accuracy. However, our RCSR specimen simulations over-predict the texture development and do not accurately predict the specimen deformation, though the deformation prediction improves when the texture is not allowed to evolve. We attribute this discrepancy to the elongated crystal morphology in the RCSR specimen which is not captured by our mean-field model.

Acknowledgements: We would like to thank Christopher Michaluk, formerly of the Cabot Co.,

for supplying the tantalum rod and helpful discussions, Carl Trujillo for performing the Taylor impact tests, and Paul Maudlin for insights on the Taylor specimen behavior. This work was partially supported by the DoD/DOE Joint Munitions Technology Development Program.

References

[1] G. I. Taylor. Testing of materials at high rates of loading. *Journal of Inst. of Civil Eng.*, 26: 486, 1946.

[2] G.I. Taylor. Plastic strain in metals. *J. Inst. Metals*, 62:307–24, 1938.

[3] S. V. Harren and R. J. Asaro. Nonuniform deformations in polycrystals and aspects of the validity of the Taylor model. *J. Mech. Phys. Solids*, 37(2):191–232, 1989.

[4] S.R. Kalidindi, C.A. Bronkhorst, and L. Anand. Crystallographic texture evolution during bulk deformation processing of FCC metals. *J. Mech. Phys. Solids*, 40:537–69, 1992.

[5] U.F. Kocks, C.N. Tomé, and H.-R. Wenk. *Texture and Anisotropy.* Cambridge University Press, 1998.

[6] Y.B. Chastel and P.R. Dawson. Equilibrium-based model for anisotropic deformations of polycrystalline materials. *Mater. Sci. Forum*, 157:1747–51, 1994.

[7] H. Honeff and H. Mecking. Analysis of the deformation texture at different rolling conditions. *Proceedings of ICOTOM 6*, 1:347–55, 1982.

[8] U.F. Kocks and H. Chandra. Slip geometry in partially constrained deformation. *Acta Metall.*, 30:695–709, 1982.

[9] P. Van Houtte. On the equivalence of the relaxed Taylor theory and the Bishop–Hill theory for partially constrained plastic deformation of crystals. *Mater. Sci. Eng.*, 55:69–77, 1982.

[10] R.A. Lebensohn and C.N. Tomé. A self-consistent anisotropic approach for the simulation of plastic deformation and texture development of polycrystals: application to zirconium alloys. *Acta Metall. Mater.*, 41:2611–24, 1993.

[11] P. Van Houtte, L. Delannay, and I. Samajdar. Quantitiative prediction of cold rolling texture in low-carbon steel by means of the lamel model. *Texture Microstruct*, 31:109–49, 1999.

[12] M. Crumbach, G. Pomana, P. Wagner, and G. Gottstein. A Taylor type deformation texture model considering grain interaction and material properties. Part I - Fundamentals. In G. Gottstein and D. A. Molodov, editors, *Recrystallization and Grain Growth, Proceedings of the First Joint Conference, Springer, Berlin*, pages 1053–60, 2001.

[13] M.R. Tonks, J.F. Bingert, C. Bronkhorst, E.N. Harstad, and D.A. Tortorelli. Two stochastic mean-field polycrystal plasticity methods. *Draft*, 2008.

[14] P Van Houtte, A. Van Bael, and J. Winters. The incorporation of texture-based yield loci into elasto-plastic finite element programs. *Texture Microstruct*, 24:255–72, 1995.

[15] P.J. Maudlin, Wright S.I., U.F. Kocks, and M.S. Sahota. An application of multisurface plasticity theory: yield surfaces of textured materials. *Acta Mater.*, 44(10):4027–32, 1996.

[16] A M Habraken and Laurent Duchene. Anisotropic elasto-plastic finite element analysis using a stress-strain interpolation method based on a polycrystalline model. *Int. J. Plasticity*, 20: 1525–60, 2004.

[17] P. Van Houtte and A. Van Bael. Convex plastic potentials of fourth and sixth rank for anisotropic materials. *Int. J. Plasticity*, 20:1505–24, 2004.

[18] K.K. Mathur and P.R. Dawson. On modeling the development of crystallographic texture in bulk forming processes. *Int. J. Plasticity*, 5:67–94, 1989.

[19] K.K. Mathur, P.R. Dawson, and U.F. Kocks. On modeling anisotropy in deformation processes involving textured polycrystals with distorted grain shape. *Mech. Mater.*, 10:183–202, 1990.

[20] A. J. Beaudoin, K. K. Mathur, P. R. Dawson, and G. C. Johnson. Three-dimensional deformation process simulation with explicit use of polycrystal plasticity models. *Int. J. Plasticity*, 9(7):833–60, 1993.

[21] Dierk Raabe and Franz Roters. Using texture components in crystal plasticity finite element simulations. *Int. J. Plasticity*, 20:339–61, 2004.

[22] P. Tugcu, K.W. Neale, P.D. Wu, and K. Inal. Crystal plasticity simulation of the hydrostatic bulge test. *Int. J. Plasticity*, 20:1603–53, 2004.

[23] T. Bohlke, G. Risy, and A. Bertram. Finite element simulation of metal forming operations with texture based material models. *Model. Simul. Mater. Sc.*, 14:365–87, 2006.

[24] D. Tikhovskiy, D. Raabe, and F. Roters. Simulation of the deformation texture of a 17% Cr ferritic stainless steel using the texture component crystal plasticity finite element method considering texture gradients. *Scripta Mater.*, 54:1537–42, 2006.

[25] M. Kothari and L. Anand. Elasto-viscoplastic constitutive equations for polycrystalline metals: application to tantalum. *J. Mech. Phys. Solids*, 46(1):51–83, 1998.

[26] U. F. Kocks, J. S. Kallend, and A. C. Biondo. Accurate representations of general textures by a set of weighted grains. Technical report, Los Alamos National Laboratory LA-UR-90-2828, Los Alamos, NM, 1990.

[27] P. J. Maudlin, J. F. Bingert, and G. T. Gray III. Low-symmetry plastic deformation in BCC tantalum: experimental observations, modeling and simulations. *Int. J. Plasticity*, 19:483–515, 2003.

[28] Y.B. Zel'dovich and Y.P. Raizer. *Physics of Shock Waves and High-Temperature Hydrodynamic Phenomena*, volume 2. Academic Press, Inc., 1967.

[29] J.M. Walsh, M.H. Rice, R.G. McQueen, and F.L. Yarger. Shock-wave compression of 27 metals - equations of state of metals. *Phys. Rev.*, 108(2):196–216, 1957.

[30] R.J. Asaro and A. Needleman. Texture development and strain hardening in rate dependent polycrystals. *Acta Metall.*, 33:923–53, 1985.

[31] R. Becker. Analysis of texture evolution in channel die compression - I. Effects of grain interaction. *Acta Metall. Mater.*, 39(6):1211–30, 1991.

[32] S. R. Kalidindi, C. A. Bronkhorst, and L. Anand. On the accuracy of the Taylor assumption in polycrystalline plasticity. In *Anisotropy and localization of plastic deformation*, pages 139–42. Elsevier appl sci publ ltd, 1991.